This article was published in Chemical Engineering Research and Design, 92, 2668-2680, 2014
http://dx.doi.org/10.1016/j.cherd.2013.12.028

# Boehmite-phenolic resin carbon molecular sieve membranes—Permeation and adsorption studies

*Miguel Teixeira* [a], *Sandra C. Rodrigues*[a], *Marta Campo*[a], *David A. Pacheco Tanaka* [a,b], *Margot A. Llosa Tanco* [a], *Luís M. Madeira*[a], *José M. Sousa*[a,c], *Adélio Mendes*[a,*]

[a] *LEPABE – Faculdade de Engenharia, Universidade do Porto, Rua Dr. Roberto Frias, 4200-465 Porto, Portugal*

[b] *Presently at Tecnalia, Parque Tecnológico de San Sebastián – Paseo Mikeletegi, 2. E-20009 Donostia, San Sebastián, Spain*

[c] *Escola da Vida e das Ciências Ambientais, Departamento de Química, Universidade de Trás-os-Montes e Alto Douro, 5001-911 Vila Real, Portugal*

## Abstract

Composite carbon molecular sieve membranes (c-CMSM) were prepared in a single dipping–drying–carbonization step from phenolic resin solutions (12.5–15 wt.%) loaded with boehmite nanoparticles (0.5–1.2 wt.%). A carbon matrix with well-dispersed $Al_2O_3$ nanowires was formed from the decomposition of the resin and dehydroxylation of boehmite. The effect of the carbon/$Al_2O_3$ ratio on the porous structure of the c-CMSM was accessed based on the pore size distribution and gas permeation toward $N_2$, $O_2$, $CO_2$, He, $H_2$, $C_3H_6$ and $C_3H_8$. c-CMSM with higher carbon/$Al_2O_3$ ratios had a more open porous structure, exhibiting higher permeabilities and lower permselectivities. c-CMSM performance was above the upper bound curves for polymeric membranes for several gas pairs, particularly for $C_3H_6/C_3H_8$ (permeability toward $C_3H_6$ of 420 barrer and permselectivity of 18.1 for a c-CMSM with carbon/$Al_2O_3$ ratio of 4.4).

Unsupported films were also prepared (carbon/$Al_2O_3$ ratio 7.3) and crushed into small flakes. Equilibrium isotherms of $H_2$, $N_2$, $O_2$, $CO_2$, $C_3H_8$ and $C_3H_6$ at 293 K were determined on these flakes to obtain the kinetic and adsorption selectivities toward gas pairs of interest; obtained adsorption and diffusion coefficients accurately predicted the permeabilities of all studied gases except $CO_2$ (experimental and predicted permeabilities of 1148 and 154 barrer, respectively).

## 1. Introduction

Membrane technologies are a cheap and clean technology for gas separation. In particular, polymer membranes have been used extensively for gas separation in the last few decades. Two key parameters characterize the separation performance of membranes: the permeability and the selectivity. The permeability characterizes the ability of the membrane to be permeated by a solute while the selectivity characterizes the ability of this membrane to discriminate the permeation transport of a species compared to the mixture (Mulder, 2000). It was recognized that these are trade-off parameters since an increase in the permeation of a given species generally origins a decrease in the selectivity and vice versa (Robeson, 2008; Rungta et al., 2012). Robeson (1991, 2008) reported the separation upper bound limit of polymer membranes for several binary gas mixtures of interest. The upper bound relation- ship for membrane gas separations correlates the log of the selectivity versus the log of the permeability of the more permeable gas for achieving the desired result of a high selectivity combined with a high permeability. Microporous membranes are capable of overcoming this upper limit since they show much higher permeabilities for equivalent selectivities. CMSM are a class of inorganic porous membranes that display the aforementioned good selectivity/permeability relationship (Campo et al., 2010a; Centeno and Fuertes, 1999, 2001; Centeno et al., 2004; Hagg et al., 2003; Kim et al., 2004; Kita et al., 1997; Lagorsse et al., 2004).

Although more expensive than polymeric membranes, they have a tunable pore size distribution and are more thermally, chemically and wear resistant. Carbon membranes have a complex pore structure that combines the sieving effects of the smaller pores with preferential adsorption on its larger ones. This bi-modal distribution can lead to high selectivities while maintaining good permeabilities (Saufi and Ismail, 2004). However, carbon membranes also have their own drawbacks, such as brittleness and their fabrication suffers from poor reproducibility (Koros and Mahajan, 2000). More- over, when exposed to air or to impurities such as large organics and water vapor they are known to exhibit a decrease in performance (Jones and Koros, 1994, 1995; Lagorsse et al., 2008; Menendez and Fuertes, 2001). It was verified that the existence of oxygen-based functional groups on the surface of the carbon membranes could enhance the adsorption of water vapor and then increase the water obstruction effect (Lagorsse et al., 2008), which limits the applicability of this type of membranes. In this context, new approaches concerning the preparation of CMSM have been proposed. Namely, the concept of composite carbon molecular sieve membranes (c- CMSM) – incorporation of nanoparticles in the carbon matrix – has appeared

as an alternative to improve the permeation performance, chemical and thermal stability of CMSM (Barsema et al., 2003, 2005; Liu et al., 2006, 2009; Park et al., 2004, 2005; Teixeira et al., 2011, 2012; Xiao et al., 2010; Yin et al., 2010; Yoda et al., 2004; Zeng et al., 2008).

Kim et al. (2002, 2003) prepared c-CMSM from metal- substituted sulfonated polyimides and observed that the permeabilities increased with the ionic radius of the metal ions (Kim et al., 2003). Barsema et al. (2003, 2005) dispersed Ag nanoparticles into P84 and P84/SPEEK precursors and observed that the O /N selectivity of the c-CMSM was higher than that of the non-functionalized CMSM. Yoda et al. (2004) reported a 17-fold enhancement of H /N selectivity of CMSM after adding Pt and Pd to polyimide precursors. Hollow-fiber CMSM derived from sulfonated poly(phenylene oxide) (SPPO) were prepared by Yoshimune et al. (2006). Metal cations such as $Na^{+}$, $Mg^{2+}$, $Al^{3+}$, $Ag^{+}$, $Cu^{2+}$ and $Fe^{3+}$ were ion-exchanged with the proton of the sulfonic acid group of SPPO and the effects on gas transport properties for the carbonized membranes investigated; Ag-SPPO membranes carbonized at 923 K had the best performance for $O_2/N_2$ separation. Park et al. (2004, 2005) reported that silica loaded c-CMSM exhibited better performances due to the fast diffusion on silica microporous domains. Novel c-CMSM has also been successfully prepared through the incorporation of nano-sized zeolites into the polymeric precursor, revealing excellent performances (Liu et al., 2006, 2009).

This work proposes the incorporation of low cost nanoparticles (boehmite) in a low cost, high carbon yield polymer (phenolic resin) to prepare a composite carbon membrane in a single dipping–drying–carbonization step. During carbonization, the polymer decomposed forming a carbon matrix with homogeneously distributed $Al_2O_3$ nanofillers, derived from the dehydration of the boehmite nanoparticles. c-CMSM with three different polymer/boehmite compositions were prepared (keeping the same carbonization conditions) and their separation properties for several gas pairs of interest dis- cussed. The decrease in performance of the c-CMSM due to air exposure (aging) was also studied.

## 2. Experimental

### *2.1. Materials*

The industrial phenolic resin was supplied by Euroresinas- Indústrias Químicas, SA. *N*-Methyl-2-pyrrolidone was provided by Acros Organics and boehmite solution by Kawaken Fine Chemicals Co. Ltd. The $\alpha$-$Al_2O_3$

tubular sup- ports were purchased from Inopor and non-porous $Al_2O_3$ tubes from Omega Engineering Limited.

The permanent gases used in this work were supplied by Air Liquide (99.999%). $C_3H_8$ and $C_3H_6$ were supplied by Praxair (99.5%).

### 2.2. *Membrane synthesis*

Tubular ceramic supports were prepared attaching porous $Al_2O_3$ supports to non-porous $Al_2O_3$ tubes bonding them with a glass sealant at 1423 K. An effective length of approximately 50 mm was left for carbon membrane adhesion.

The precursors were prepared by mixing an industrial phenolic resin diluted in *N*-methyl-2-pyrrolidone (NMP) with a 10 wt.% aqueous dispersion of boehmite nanoparticles (particle size, 8–20 nm). Table 1 lists the composition of the prepared dispersions used to prepare the c-CMSM. After the preparation of the precursor, supported membranes were obtained by dip coating assisted with a vacuum pump. The membranes were dried in a rotating oven at 313 K for 2 h to avoid a quick release of the solvent that could cause the formation of cracks/defects. Subsequently, they were left to dry overnight at 363 K. The supported membranes were finally carbonized inside a tubular horizontal furnace at 823 K under a $N_2$ atmosphere (flow rate 100 mL $min^{-1}$). A soaking time of 2 h and a heating rate of 274 K $min^{-1}$ were used (Teixeira et al., 2011, 2012). Fig. 1 shows a photograph of an obtained supported c-CMSM. It can be observed a uniform and well-adhered carbon membrane to the $Al_2O_3$ support. These supported membranes were used for permeation studies. Additionally, free films of these solutions were prepared following a similar procedure as for the supported carbon membranes and then crushed into flakes for characterization/adsorption studies.

### 2.3. *Morphological and structural characterization of* the membranes

Mass loss values were determined in a Netzsch TG 209 F1 Iris thermogravimetric balance (resolution 0.1 $\mu$m). Characteristic curves were determined under $N_2$ atmosphere in the temperature range 293–1173 K (heating rate 283 K $min^{-1}$). The mass loss of membrane M1 was previously determined (Teixeira et al., 2011). The carbon and $Al_2O_3$ contents in the final carbon film were 88 wt.% and 12 wt.%, respectively. Scanning electron microscopy (SEM) was used to analyze the cross section of the carbonized membranes and determine

the composite layer thickness and energy dispersive X-ray spectroscopy (EDS) was used to achieve a qualitative elemental composition of the carbon membranes. SEM/EDS analysis was performed at high vacuum in a FEI Quanta 400 FEG/EDAX Genesis X4M microscope with 1.2 nm resolution.

### 2.4. *Permeation experiments*

Mono and bicomponent permeabilities were determined in a shell and tube membrane apparatus. Gases with different kinetic diameters were selected: He (0.260 nm), $H_2$ (0.290 nm), $CO_2$ (0.33 nm), $O_2$ (0.346), $N_2$ (0.364), $C_3H_6$ (0.40 nm) and $C_3H_8$ (0.43 nm) (Breck, 1974). Fig. 2 shows a scheme of the experimental setup used for these experiments. The gas/mixture stream was fed at 200–500 kPa (pressure controlled by means of a Horiba Stec UR-7340 pressure controller) at the shell side, while the tube (permeate) side was kept at 100 kPa. The permeating flow rate of the gas/mixture was measured using mass flow meters (El-Flow Bronkhorst, ranges 0–1, 0–10 and 0–100 mLN $min^{-1}$). For mixed gas permeation experiments, a stainless steel tank connected to a pressure sensor (Druck series PMP 4010, range 0–700 kPa, accuracy 0.04% full scale) was used to prepare equimolar $C_3H_6/C_3H_8$ mixtures and a mass flow controller (El-Flow Bronkhorst, 0–1 LN $min^{-1}$) was used to set the retentate flow rate at about ten times the value of the permeating flow rate, to guarantee that the feed composition in the shell was uniform. The accuracy of the Bronkhorst mass flow meters/controllers was ±0.8% RD (read value error) plus ±0.2% FS (full scale error).

An acquisition board (Advantech 8710 HG) was used to acquire the signal from the pressure sensors and mass flow meters/controllers and a Labview program was used for signal treatment. The compositions of the feed and permeating streams were determined using a GC (Dani 1000) equipped with a ValcoPlot column (VP 30 m × 53 mm × 20 $\mu$m), a FID 86/10 detector and a split/splitless injector. The temperatures used in the column, detector and injector were 353, 523 and 393 K, respectively.

### 2.5. *Adsorption isotherms/uptake experiments*

Flakes of membrane M1 were used in all adsorption and uptake experiments.

To characterize a microporous material, the most used method is the adsorption of $N_2$ at 77 K. However, when ultra- microporosity is present diffusional restrictions occur and the use of $CO_2$ at 273 K is a good alternative to

overcome these limitations (Teixeira et al., 2011; Campo et al., 2010b). Adsorption isotherm of $CO_2$ at 273 K and the adsorption isotherms of $H_2$, $CO_2$, $O_2$, $N_2$, $C_3H_8$ and $C_3H_6$ at 293 K were obtained in a Rubotherm® magnetic suspension balance with a precision of 10 $\mu$g (Campo et al., 2010b). The adsorption kinetics of each equilibrium point was used to determine the gas diffusivities (uptake curves). Before use and whenever the adsorbed gas was changed, the adsorbent samples were degassed in cycles of high-pressure helium and vacuum (ca. 10 Pa) for up to 36 h at 343 K.

All the experiments were performed with at least 3 samples prepared in the same conditions. In this way, the obtained results are averages based on the measurements of all replicates.

## 3. Results and discussion

### *3.1. Morphological and structural analyses*

Thermogravimetric analyses were conducted from 293 to 1173 K and Table 2 lists the burn off percentages for M1, M2 and M3 as well as their composition. The contents of carbon and $Al_2O_3$ of membranes M2 and M3 could be estimated because the composition of M1 had been previously determined by proximate analysis (Teixeira et al., 2011). The mass loss is similar for both membranes, hence their carbonaceous structure is also similar. The burn off of M1 (higher carbon/$Al_2O_3$ ratio-cf. Table 2) is slightly higher because the mass loss of the phenolic resin during carbonization is larger than the mass loss due to the dehydroxylation of boehmite to $Al_2O_3$. Yet, these burn off differences between the membranes are not too significant.

Fig. 3 shows SEM cross sectional images of the composite membrane M1; a ca. 2.5 $\mu$m thick uniform composite layer can be observed on top of the $\alpha$-$Al_2O_3$ support tube. EDS analysis (data not shown) revealed that the white patches observed in Fig. 3 correspond to Barium, a common component of industrial phenolic resins. It was also observed that $Al_2O_3$ was uniformly distributed throughout the membrane.

The thickness of membranes M2 and M3 was approximately the same of M1 (2.5 $\mu$m), thus the resin/boehmite ratio had little impact on the membranes thickness.

The microporosity of the material was studied by adsorption of $CO_2$ at 273 K and the Dubinin–Raduschkevisch (DR) (Dubinin and Astakhov, 1971a,b; Dubinin et al., 1973) equation (Eq. (1)) was used to fit the experimental results:

$$\frac{W}{W_0} = \exp^{[-((\Re T \ln(P_0/p))/E)^2]}, \quad (1)$$

where $W$ refers to the micropore volume filled at pressure $P$, $W0$ is the total micropore volume, $E$ the characteristic energy, $P0$ the vapor pressure of the free liquid, $\mathcal{R}$ is the gas constant and $T$ is the absolute temperature.

Fig. 4 presents the characteristic curves for all studied c- CMSM.

For all membranes, a good agreement of the DR equation fitting with the characteristic curve is observed; the slope of the plot is related to the characteristic energy of the micropore and the intersect is related to the micropore volume. Furthermore, Stoeckli' correlation was used to estimate the average micropore width ($\ell$) (Stoeckli and Centeno, 1997; Stoeckli et al., 2002):

$$\ell = \frac{10.8}{E_0 - 11.4} \quad (2)$$

Table 3 summarizes the structural parameters determined. It is observed that an increase in Al2O3 content leads to an increase in both the total micropore volume and average pore width.

In order to acquire a more detailed knowledge of the porous structure of the c-CMSM, their pore size distribution (PSD) was determined using the structure-based method developed by Nguyen et al. (Campo et al., 2010b; Nguyen and Do, 1999; Nguyen et al., 2003). Fig. 5 shows the resulting pore size distributions.

The PSD of membrane M1 features a higher amount of smaller micropores (below 0.5 nm) than membranes M2 and M3, which in turn exhibit a higher amount of the larger micropores (higher than 0.5 nm). Moreover, the number of larger micropores increases as the Al2O3 content increases (from membrane M1 to M3). It can be observed that boehmite nanoparticles play a role on the exhibited porosity of the membranes (opens the c-CMSM porous structure) and above a certain concentration of boehmite a bi-disperse porosity is observed.

### 3.2. *Permeation experiments*

#### 3.2.1. *Effect of the composition of c-CMSM on gas* permeation properties

Gas permeation experiments were carried out at 293 K. The permeability of the c-CMSM toward a species was determined from:

$$L_i = \frac{J_i \delta}{\Delta P}, \quad (3)$$

where $L_i$ is the permeability, $J_i$ the permeating flux, $\varepsilon$ the membrane thickness and $L'P$ the driving force. The permeability was expressed in Barrer, which equals to $3.35 \times 10^{-16}\,\mathrm{mol\,m\,m^{-2}\,s^{-1}\,Pa^{-1}}$.

The permselectivity ($S$), often shortened to selectivity, is the ratio of the two permeability coefficients ($i$ and $j$):

$$S = \frac{L_i}{L_j} \quad (4)$$

The permeabilities and ideal selectivities of membranes M1–M3 for several gases are summarized in Tables 4 and 5.

Fig. 6 illustrates the effect of the ratio carbon/$Al_2O_3$ on the gas separation properties of the carbonized mem- branes. Membrane permeabilities and ideal selectivies for $O_2/N_2$, $CO_2/N_2$, $He/N_2$ and $C_3H_6/C_3H_8$ as a function of the carbon/$Al_2O_3$ ratio are shown in Fig. 6A and B, respectively.

Fig. 6A shows that when the carbon/$Al_2O_3$ ratio is lower, the membrane permeabilities toward the probe gases are higher; this increase in permeability (M3 > M2 > M1) is consistent with the increase in average pore size as the carbon/$Al_2O_3$ ratio decreases (cf. PSDs shown in Fig. 5). However, this increase is not very significant for smaller molecules (e.g. He and $CO_2$) yet very significant for larger molecules (e.g. $C_3H_6$ and $C_3H_8$) Molecules such as He and $CO_2$ likely access almost all the ultramicropores (constrictions) of membrane M1 so the permeability toward these gases increases only slightly upon increase of the pore size (M1 → M2 → M3). On the other hand, molecules with diameters closer to the size of the constrictions are either blocked/diffuse slowly in the porous matrix of membrane M1, hence the increase in permeability upon increase in pore size is much bigger (up to 25 and 40-fold for $C_3H_6$ and $C_3H_8$, respectively). This also accounts for the increase in the ideal selectivities as the pore size of the membrane decreases (cf. Fig. 6B).

These results are consistent with the behavior observed by Robeson for the performance of polymeric membranes (Robeson, 1991); an increase in selectivity occurs at the expense of a decrease in permeability and vice versa. The results obtained were inserted into the semi-empirical plots devised by Robeson (2008) (and Burns and Koros (2003) for the $C_3H_6/C_3H_8$ separation). Fig. 7 illustrates the upper bound limits for $O_2/N_2$, $H_2/N_2$, $CO_2/N_2$, $H_2/CO_2$ and $C_3H_6/C_3H_8$. These

plots are widely acknowledged as the state-of-the art curves for each gas separation.

The results for $O_2/N_2$, $H_2/CO_2$ and $CO_2/N_2$ separation are slightly below or slightly over the Robeson upper bound for all membranes. However, the results for $H_2/N_2$ and $C_3H_6/C_3H_8$ are clearly above the upper bound plots. The use of these composite membranes for the $C_3H_6/C_3H_8$ separation is of particular interest, given the high costs of its current industrial separation process (distillation).

Hence, $C_3H_6/C_3H_8$ mixed gas experiments were carried out with membranes M2 and M3 using equimolar feeds (the total pressures in the feed and permeate were the same as the ones used in single gas experiments). The steady state permeation results achieved are plotted together with the single gas results in Fig. 7E. The separation factors obtained are below the ideal selectivity values and the permeability toward both hydrocarbons decreases. This result is consistent with the findings of Chng et al. (2009). These results imply that the interactions between the molecules of $C_3H_8$ and $C_3H_6$ differ from $C_3H_8/C_3H_8$ or $C_3H_6/C_3H_6$ interactions. In a mixture feed, $C_3H_8$ and $C_3H_6$ should impact negatively the diffusion of each other to the constrictions, causing a decrease in permeability. This competition causes a bigger decrease in the diffusion of $C_3H_6$, the faster species, so selectivity also decreases.

#### 3.2.2. *Stability in air and regeneration*

After gas permeation experiments, membrane M2 was exposed for 8 days to ambient air (humidity not controlled). Afterwards, the membrane permeability toward $N_2$ was re- determined. The permeability toward $N_2$ was 5% of the value measured for the fresh membrane, indicative of fast pore clogging with water vapor (Lagorsse et al., 2008). However, after in situ regeneration at 673 K for 4 h in $N_2$ atmosphere, the membrane permeability toward $N_2$ was 75% of its initial value. This process (8 days exposure to ambient air and subsequent regeneration at 673 K) was repeated and the same permeability value was determined, displaying cyclic behavior.

At the moment, passivation treatments with hydrogen are being studied to decrease the hydrophilic nature of the surface of the CMSM and improve their long-term stability.

### 3.3. *Adsorption isotherms*

The adsorption equilibrium isotherms (and the correspondent uptake curves) were used to determine the kinetic and adsorption selectivities for the following

gas pairs: O2/N2, CO2/N2, H2/CO2, H2/N2 and C3H6/C3H8. The adsorption equilibrium isotherms curves of O2, N2, H2, CO2, C3H6 and C3H8 were determined on c-CMSM flakes of membrane M1 at 293 K over the pressure range 0–700 kPa. The experimental data was fitted to the Langmuir and SIPS equations (Eqs. (5) and (6), respectively) (Do, 1998; Campo et al., 2010b; Lagorsse et al., 2004):

$$q = q^{\max}\frac{bP}{1+bP}, \tag{5}$$

$$q = q^{\max}\frac{(bP)^{1/n}}{1+(bP)^{1/n}}, \tag{6}$$

where $q$ is the gas adsorbed amount (mol $kg^{-1}$), $q^{\max}$ is the adsorption saturation capacity, $b$ is the equation parameter ($kPa^{-1}$), $P$ is the pressure (kPa) and $n$ is a parameter that characterizes the system heterogeneity; the larger is this parameter, the more heterogeneous is the system (Do, 1998). When $n$ is equal to 1, the SIPS equation becomes the Langmuir equation. Fig. 8 shows both the experimental data (symbols) and the respective fittings (lines).

It can be observed that CO2 is the most adsorbable among the permanent gases due to its induced polarity and small size. Adsorption isotherms of the hydrocarbon gases on c- CMSM are of type I; the same type of adsorption isotherm was observed by other authors (Okamoto et al., 1999). Propane and propylene began adsorbing more than CO2 but due to their bulkier size end to adsorb less for higher pressures. Also, propylene adsorbs more than propane for higher pressure probably because its smaller size, which allow it to enter as well into smaller pores.

Table 6 summarizes the Langmuir and SIPS isotherm parameters, calculated by minimizing the fitting error, *Err*, defined as:

$$Err = \frac{1}{n_v}\sum_{i=1}^{n_v}\left(\frac{q_i^{model}-q_i^{\exp}}{q_i^{\exp}}\right)^2, \tag{7}$$

where $nv$ refers to the number of experimental values, $q^{exp}$ is the adsorbed concentration and $q^{mod}$ is the adsorbed concen- tration given by the model. To determine the most adequate model a model selection criterion (MSC) was used (Brandao et al., 2004):

$$\mathrm{MSC} = \ln\left(\frac{\sum_{i=1}^{m}(q_i^{exp} - q_{avg}^{exp})^2}{\sum_{i=1}^{m}(q_i^{exp} - q_i^{model})^2}\right) - 2\frac{n_p}{n_v}, \quad (8)$$

where $q_{avg}^{exp}$ is the average of all experimental $q$ values for a given gas and $np$ is the number of parameters of each model. The model selection criterion weights the deviation to the experimental values as well as the number of fitting parameters and both are minimized for higher MSC values.

Table 6 shows that the SIPS equation fits better the adsorption isotherm for all six gases, displaying higher MSC values and lower fitting errors. Besides the adsorption equilibrium conditions, the transient uptake curves of all gases were also determined and the apparent diffusivity coefficients computed. The mass uptake at any time t was normalized by the mass uptake at equilibrium ($t = \infty$) and the fractional uptake was calculated as

$$F = \frac{m_t - m_0}{m_\infty - m_0}, \quad (9)$$

where $m0$ is the mass at $t = 0$.

The fractional uptake was correlated to the apparent diffusivity coefficients given by a suitable model. When the uptake is controlled by micropore diffusion the fractional uptake is expressed by Eq. (10) (Do, 1998) for a slab geometry

$$F = 1 - \frac{2}{\pi^2}\sum_{v=1}^{\infty}\frac{1}{(v-0.5)^2}\exp\left(-(v-0.5)^2\pi^2\frac{D}{\Lambda^2}t\right), \quad (10)$$

where $\Lambda$ is half of the slab thickness (measured with a caliper) and $D$ is the diffusivity coefficient. On the other hand, when the gas diffusion is controlled by the pore mouth barrier, a LDF (linear driving force) model is used instead (Rutherford and Coons, 2005), represented by Eq. (11) (Glueckauf, 1955), where k represents a mass transfer coefficient.

$$F = 1 - \exp(-kt) \quad (11)$$

Fig. 9 shows the plots of the uptake curves for $N_2$ and $O_2$ at 15 and 35 kPa, respectively. It can be seen that the micropore diffusion model provides a better depiction of the uptake behavior at high times. Yet, at low time values, the experimental curves are not perfectly described by either model. This suggests the mass transport is being con- trolled by a combined effect of the diffusion in the pore mouth and micropores. Therefore, a pore mouth/micropore diffusion model would probably provide a more accurate depiction of the uptake behavior. Since the implementation of this model would require some computation effort and because at higher times the fitting provided by the micro- pore diffusion model was much better, it was considered that the mass transport was controlled by the diffusion in the micropores.

For $O_2$, an initial fast uptake ($F$ appears to reach a plateau at 2000 s) is followed by a very slow increase, and the system is not at equilibrium even after 72 h. This behavior is consistent with chemisorption and Elovich's kinetic law has been reported to describe the uptake of chemisorption phenomena (Mclintoc, 1967):

$$r_c = \frac{dF_c}{dt_c} = \xi \exp(-\zeta F_c), \qquad (12)$$

where $r_c$ is the rate of $O_2$ chemisorption, $t_c$ is the chemisorption time and $\xi$ and $\zeta$ are model constants. Finally, $F_c$ is chemisorption uptake, i.e. the experimental uptake after subtracting the physical adsorption to the total amount adsorbed. Fig. 10 illustrates the uptake chemisorption history of $O_2$ for three different oxygen partial pressures. It can be observed that Elovich equation describes well the experimental chemisorption uptake rate, confirming $O_2$ chemisorption occurs. The decrease in the amount adsorbed for higher pressures is also indicative of chemisorption.

Hence, the diffusivity of $O_2$ was determined using the physical adsorption data values. Because $O_2$ chemisorbs on the c-CMSM, its desorption isotherm curve was also determined. Fig. 11 plots both the adsorption and desorption branches of the isotherm curve of $O_2$, which took approximately 3 weeks to obtain. Unsurprisingly, around 10% of the $O_2$ adsorption capacity was not restored. This is consistent with the findings by Lagorsse et al. (2008), whom studied $O_2$ chemisorption in hollow fiber CMSM. Additionally, Lagorsse et al. (2008) observed that vacuum in situ regenerations at 343 K were unsuccessful to restore the original $O_2$ adsorption capacity. So, the adsorbent was regenerated in situ at 343 K in a He atmosphere for two days followed by determination of the adsorption capacity toward $N_2$ (instead of $O_2$). Interestingly, the adsorption

capacity of the regenerated c-CMSM sample toward N2 was the same as that of the fresh sample, indicating that the relevant adsorption area for N2 did not change much.

### 3.3.1. *Pressure dependence of diffusivity coefficients*

The Darken relation is one of the most used to describe the pressure dependence of diffusivity coefficients. It is derived considering that the driving force for the mass transport is the chemical potential gradient. According to the Darken equation and assuming ideal gas behavior the diffusivity coefficients are given by (Do, 1998):

$$D = D_0 \frac{\partial \ln P}{\partial \ln q}, \tag{13}$$

where $D_0$ is the diffusivity at zero loading. For a SIPS isotherm, it becomes:

$$D = D_0 n(1 + (bP)^{1/n}) = D_0 \frac{n}{1-\theta} = \frac{D_0'}{1-\theta}, \tag{14}$$

where $\theta$ is the fractional loading.

This equation was used to fit the dependence of the diffusivity coefficients with pressure (loading). Fig. 12A represents the pressure dependence of the diffusivities for the permanent gases (O2, N2 and CO2) and Fig. 12B the same dependence for the hydrocarbons (C3H6 and C3H8). Accurate values of H2 diffusivities could not be determined because it diffused too quickly.

Fig. 12A shows that the N2 diffusivities obey to the Darken- SIPS relationship but the diffusivities of CO2 and O2 at higher loadings are lower than those predicted by the Darken relation. Chen and Yang (1991) have previously reported this behavior, attributing it to the pore blocking effect caused by adsorbed molecules. Since Darken relation predicts always that diffusivity increases with loading, these authors proposed a new model that features an additional parameter ($\lambda$) to account for the effect of the pore blocking:

$$D = D_0' \frac{1 - \theta + \lambda/2\theta(2-\theta) + H(1-\lambda)(1-\lambda)\lambda/2\theta^2}{(1 - \theta + \theta\lambda/2)^2}, \tag{15}$$

where $H$ is the Heaviside function. This behavior was first evidenced in CMS unsupported membranes by Campo et al. (2010b). Fig. 12A shows that this model described well the diffusivities of O2 and CO2 as a function of pressure. Fig. 12A also shows that the order of the diffusivities O2 > CO2 > N2 does not follow the order of the kinetic diameters CO2 < O2 < N2 (Breck, 1974), which is consistent with other reports in the literature (Bae and Lee, 2005; Reid and Thomas, 1999;

Rutherford and Do, 2000). However, differences in molecular shape are just as important. The 3D structure of a molecule impacts on its rotational, translational and vibrational degrees of movement in the constrictions (Singh and Koros, 1996). More- over, gas electronic properties, which influence the specific adsorbate–adsorbent interactions, have also been reported to affect the gas diffusivity (Bae and Lee, 2005).

On the other hand, the diffusivities of $C_3H_6$ and $C_3H_8$ exhibit a stronger pressure-dependence than predicted by the Darken relation-cf. Fig. 12B. Do (1996) have proposed a structural-diffusion model for gases that exhibit this stronger dependence

$$D = \frac{A}{dq/dP}, \tag{16}$$

where $A$ is a constant.

For a SIPS isotherm, the relation becomes:

$$D = D_0' \frac{(1 + (bP)^{1/n})^2}{(bP)^{(1-n)/n}} \tag{17}$$

Fig. 12B shows that the structural-diffusion model (Do- SIPS) describes well the experimental results of $C_3H_6$ and $C_3H_8$.

### 3.3.2. Experimental and predicted permeabilities

From the adsorption equilibrium and diffusivity values obtained, adsorption and diffusion selectivities for the gas pairs $O_2/N_2$, $CO_2/N_2$ and $C_3H_6/C_3H_8$ in the pressure range 100–700 kPa were computed. Fig. 13 shows the adsorption (Fig. 13A) and diffusion (Fig. 13B) coefficients ratio for the referred gas pairs as a function of the pressure. The adsorption and diffusion coefficients of each gas correspond to the best fitting models of the equilibrium isotherm and adsorption uptake experiments. This c-CMSM sample exhibits adsorption and diffusion selectivity for $O_2/N_2$ separation, mostly adsorption selectivity for $CO_2/N_2$ separation and mostly diffusion selectivity for $C_3H_6/C_3H_8$ separation.

The experimental permeation results of membrane M1 were compared with the permeabilities (and permselectivities) predicted from the adsorption and diffusion coefficients determined.

The surface-diffusion model was used to relate the permeating flux ($J_i$) across the membrane with the Fickian diffusivity ($D$) and adsorbed capacity ($q$)

$$J_i = -D_i \rho_s \frac{dq}{dz}, \qquad (18)$$

where $\rho_S$ is the skeleton density of the material (Teixeira et al., 2011) and $z$ is the spatial coordinate of the membrane (zero at retentate surface and $\delta$ at permeate surface). Since the permeability ($L_i$) is expressed as the ratio between the permeating flux and the driving force, normalized by the membrane thickness (cf. Eq. (3)) and $q = q^{\max}\theta$ and $D = D^{\ddagger}_{\theta} f(\theta)$, one can determine the permeability coefficients for each component $i$ applying the following equation:

$$L_i = \frac{-q_i^{\max} \rho_s D'_{0,i}}{\Delta P_i} \int_{\theta_i, z=0}^{\theta_i, z=\delta} f(\theta_i) d\theta, \qquad (19)$$

where $f(\theta)$ has different expressions depending on the fitting model used for the diffusivities (cf. Eqs. (14), (15) and (17)).

These expressions can be found in Appendix.

Fig. 14 shows the predicted O2/N2, CO2/N2 and C3H6/C3H8 permselectivities as a function of the feed pressure. These permselectivities were determined integrating Eq. (18). It can be observed that the C3H6/C3H8 permselectivity is the same (18.9) regardless of the feed pressure and that the permselectivity toward the O2/N2 does not depend much on the pressure, ranging from 3.6 to 3.9 for the feed pressure range 100–700 kPa. On the other hand, the CO2/N2 permselectivity decreases significantly with pressure (from 7 at 700 kPa to 2.7 at 270 kPa) because the CO2/N2 ratio of the sorption coefficients is significantly higher at lower pressures (cf. Fig. 13A).

Table 7 shows the permeabilities (and permselectivities) determined experimentally for M1 and compares it with the predicted values from adsorption/diffusion studies. The permeation values were determined in steady-state conditions and only gas diffusion in wall-to-wall pores was relevant. Meanwhile, in adsorption experiments the diffusion coefficients are calculated by fitting the transient uptake curve, which is affected by the diffusion of the molecules in both the dead-end pores and wall-to-wall pores.

The permeabilities determined from both methods are similar for O2, N2, C3H6 and C3H8, and only significantly different for CO2. These results show that the dead end pores are likely only accessible to CO2, thus not affecting the

permeability results of the other larger gases.

## 4. Conclusions

Phenolic resin-based composite carbon molecular sieve mem- branes (c-CMSM) loaded with boehmite nanoparticles were prepared as supported membranes for permeation studies and as free films for adsorption equilibrium/kinetic studies. Membranes were prepared from solutions with varying phenolic resin and boehmite compositions, leading to the formation of c-CMSM membranes with different carbon/$Al_2O_3$ ratios. It was observed that an increase in the carbon/$Al_2O_3$ ratio led to c-CMSM with higher volume of micropores and higher average length of these micropores. Consequently, the membranes with higher carbon/$Al_2O_3$ ratio exhibited higher permeabilities toward the probe gases and lower permselectivities. Aging effects were observed after 8 days of exposure to ambient air, but treatment in $N_2$ atmosphere at 673 K regenerated 75% of the membrane's initial performance.

The performance of the c-CMSM was above the upper bound curve for polymeric membranes for several gas pairs, notably for $C_3H_6/C_3H_8$, thus making it promising for olefin purification.

Adsorption isotherms and diffusion uptake rates for $N_2$, $O_2$, $CO_2$, $C_3H_6$ and $C_3H_8$ were determined at 293 K; the CMSM exhibited adsorption and diffusion selectivity for $O_2/N_2$ separation, mostly adsorption selectivity for $CO_2/N_2$ separation and diffusion selectivity for $C_3H_6/C_3H_8$ separation.

The adsorption and diffusion coefficients determined from adsorption equilibrium experiments showed to be adequate to predict the permeabilities of all probe gases studied with the exception of $CO_2$.

## Acknowledgments

Miguel Teixeira and Margot Tanco are grateful to the Portuguese Foundation for Science and Technology (FCT) for their doctoral grants (references SFRH/BD/24768/2005 and SFRH/BD/61898/2009, respectively). Marta Campo also acknowledges FCT for her post-doctoral grant (reference SFRH/BPD/65377/2009). The authors also acknowledge financing from FCT through the projects POCTI/EQU/59344/2004, POCTI/EQU/59345/2004 and PTDC/EQU-EQU/114944/2009.

Finally, the authors are thankful to CEMUP for the SEM analyses (REEQ/1062/CTM/2005 and REDE/1512/RME/2005 funding provided by FCT).

**Appendix.**

Permeability coefficient for C3H6 and C3H8 obtained using Do- SIPS fitting model for the diffusivities (Do, 1996):

$$L_i = \frac{q^{max,i}\rho_s b_i D'_{0,i}}{n_i}$$

Structural model constant

$$A = \frac{q^{max,i} b_i D'_{0,i}}{n_i}$$

Permeability coefficient for N2 obtained using Darken-SIPS fitting model for the diffusivities (Do, 1998):

$$L_i = \frac{q^{max,i}\rho_s D_{0,i} n_i}{\Delta p_i} \ln\left[\frac{q^{max,i} - q^{l,i}}{q^{max,i} - q^{h,i}}\right],$$

where $q^h$ and $q^l$ are the adsorbed amounts at the high ($h$) and low ($l$) pressure sides of the membrane.*f(θ) expression according Darken-SIPS fitting model:*

$$f(\theta_i) = \frac{1}{1-\theta_i}$$

Permeability coefficient for CO2 and O2 obtained using Chen–Yang fitting model for the diffusivities (Chen and Yang, 1991):

$$L_i = \frac{q^{max,i}\rho_s D'_{0,i}}{\Delta p_i}\left\{\left(\frac{4\ln(abs(\theta_{i,l}(\lambda-2)+2))(\lambda^2-\lambda+2)}{(\lambda-2)^3} + \frac{4\lambda^2}{(\theta_{i,l}(\lambda-2)+2)(\lambda-2)^3} - \frac{2\theta_{i,l}\lambda}{(\lambda-2)^2}\right) - \left(\frac{4\ln(abs(\theta_{i,h}(\lambda-2)+2))(\lambda^2-\lambda+2)}{(\lambda-2)^3} + \frac{4\lambda^2}{(\theta_{i,h}(\lambda-2)+2)(\lambda-2)^3} - \frac{2\theta_{i,h}\lambda}{(\lambda-2)^2}\right)\right\}$$

*f (θ) expression according Chen–Yang fitting model:*

$$f(\theta_i) = \frac{1-\theta_i + \lambda/2\theta_i(2-\theta_i) + H(1-\lambda)(1-\lambda)\lambda/2\theta_i^2}{(1-\theta_i+\theta_i\lambda/2)^2}$$

For $\lambda >= 1$ it reduces to

$$f(\theta_i) = \frac{1-\theta_i + \lambda/2\theta_i(2-\theta_i)}{(1-\theta_i+\theta_i(\lambda/2))^2}$$

*Integrating f (θ) it becomes:*

$$\int f(\theta_i)\,d\theta = \frac{4\ln(abs(\theta_i(\lambda-2)+2))(\lambda^2-\lambda+2)}{(\lambda-2)^3} + \frac{4\lambda^2}{(\theta_i(\lambda-2)+2)(\lambda-2)^3} - \frac{2\theta_i\lambda}{(\lambda-2)^2}$$

**References**


Bae, Y.S., Lee, C.H., 2005. Sorption kinetics of eight gases on a carbon molecular sieve at elevated pressure. Carbon 43, 95–107.

Barsema, J.N., Balster, J., Jordan, V., van der Vegt, N.F.A., Wessling, M., 2003. Functionalized carbon molecular sieve membranes containing Ag-nanoclusters. J. Membr. Sci. 219, 47–57.

Barsema, J.N., Van der Vegt, N.F.A., Koops, G.H., Wessling, M., 2005. Ag-functionalized carbon molecular-sieve membranes based on polyelectrolyte/polyimide blend precursors. Adv. Funct. Mater. 15, 69–75.

Brandao, L., Fritsch, D., Madeira, L.M., Mendes, A.M., 2004. Kinetics of propylene hydrogenation on nanostructured palladium clusters. Chem. Eng. J. 103, 89–97.

Breck, D.W., 1974. Zeolite Molecular Sieves, Structure, Chemistry and Use. John Wiley & Sons, New York.

Burns, R.L., Koros, W.J., 2003. Defining the challenges for C3H6/C3H8 separation using polymeric membranes. J. Membr. Sci. 211, 299–309.

Campo, M.C., Magalhaes, F.D., Mendes, A., 2010a. Carbon molecular sieve membranes from cellophane paper. J. Membr. Sci. 350, 180–188.

Campo, M.C., Magalhaes, F.D., Mendes, A., 2010b. Comparative study between a CMS membrane and a CMS adsorbent: Part I—Morphology, adsorption equilibrium and kinetics. J. Membr. Sci. 346, 15–25.

Centeno, T.A., Fuertes, A.B., 1999. Supported carbon molecular sieve membranes based on a phenolic resin. J. Membr. Sci. 160, 201–211.

Centeno, T.A., Fuertes, A.B., 2001. Carbon molecular sieve membranes derived from a phenolic resin supported on porous ceramic tubes. Sep. Purif. Technol. 25, 379–384.

Centeno, T.A., Vilas, J.L., Fuertes, A.B., 2004. Effects of phenolic resin pyrolysis conditions on carbon membrane performance for gas separation. J. Membr. Sci. 228, 45–54.

Chen, Y.D., Yang, R.T., 1991. Concentration-dependence of surface-diffusion and zeolitic diffusion. AIChE J. 37, 1579–1582.

Chng, M.L., Xiao, Y.C., Chung, T.S., Toriida, M., Tamai, S., 2009. Enhanced propylene/propane separation by carbonaceous membrane derived from poly(aryl ether ketone)/2,6-bis(4-azidobenzylidene)-4-methyl-cyclohexanone interpenetrating network. Carbon 47, 1857–1866.

Do, D.D., 1996. A model for surface diffusion of ethane and propane in activated carbon. Chem. Eng. Sci. 51, 4145–4158.

Do, D.D., 1998. Adsorption Analysis: Equilibria and Kinetics. Imperial College Press, London.

Dubinin, M.M., Astakhov, V.A., 1971a. Development of ideas of volume filling of micropores during adsorption of gases and vapours by microporous adsorbents. 1. Carbonaceous adsorbents. Izvestiya Akademii Nauk Sssr-Seriya Khimicheskaya, 5–10.

Dubinin, M.M., Astakhov, V.A., 1971b. Development of ideas of volume filling of micropores during adsorption of gases and vapours by microporous adsorbents. 2. General fundamentals of theory of gas and vapour adsorption on zeolites. Bull. Acad. Sci. USSR Ch+, 11.

Dubinin, M.M., Zolotare, P.p., Nikolaev, K.M., Polyakov, N.S., Petrova, L.I., Radushke, L.v., 1973. Study of adsorption dynamics in broad range of brake down concentrations. 4.Theoretical analysis of experimental-data. Izvestiya Akademii Nauk Sssr-Seriya Khimicheskaya, 293–297.

Glueckauf, E., 1955. Theory of chromatography. 10. Formulae for diffusion into spheres and their application to chromatography. Trans. Faraday Soc. 51, 1540-1551.

Hagg, M.B., Lie, J.A., Lindbrathen, A., 2003. Carbon molecular sieve membranes – a promising alternative for selected industrial applications. Adv. Membr. Technol. 984, 329–345.

Jones, C.W., Koros, W.J., 1994. Carbon molecular-sieve gas separation membranes. 2. Regeneration following organic-exposure. Carbon 32, 1427–1432.

Jones, C.W., Koros, W.J., 1995. Characterization of ultramicroporous carbon membranes with humidified feeds. Ind. Eng. Chem. Res. 34, 158–163.

Kim, Y.K., Park, H.B., Lee, Y.M., 2002. Synthesis and characterization of metal-containing sulfonated polyimide membranes and their gas separation properties. Desalination 145, 389–392.

Kim, Y.K., Park, H.B., Lee, Y.M., 2003. Carbon molecular sieve membranes derived from metal-substituted sulfonated polyimide and their gas separation properties. J. Membr. Sci. 226, 145–158.

Kim, Y.K., Park, H.B., Lee, Y.M., 2004. Carbon molecular sieve membranes derived from thermally labile polymer containing blend polymers and their gas separation properties. J. Membr. Sci. 243, 9–17.

Kita, H., Maeda, H., Tanaka, K., Okamoto, K., 1997. Carbon molecular sieve membrane prepared from phenolic resin. Chem. Lett. 1997, 179–180.

Koros, W.J., Mahajan, R., 2000. Pushing the limits on possibilities for large scale gas separation: which strategies? J. Membr. Sci. 175, 181–196.

Lagorsse, S., Magalhaes, F.D., Mendes, A., 2004. Carbon molecular sieve membranes – sorption, kinetic and structural characterization. J. Membr. Sci. 241, 275–287.

Lagorsse, S., Magalhaes, F.D., Mendes, A., 2008. Aging study of carbon molecular sieve membranes. J. Membr. Sci. 310, 494–502.

Liu, Q.L., Wang, T.H., Liang, C.H., Zhang, B., Liu, S.L., Cao, Y.M., Qiu, J.S., 2006. Zeolite married to carbon: a new family of membrane materials with excellent gas separation performance. Chem. Mater. 18, 6283–6288.

Liu, Q.L., Wang, T.H., Guo, H.C., Liang, C.H., Liu, S.L., Zhang, Z.G., Cao, Y.M., Su, D.S., Qiu, J.S., 2009. Controlled synthesis of high performance carbon/zeolite T composite membrane materials for gas separation. Microporous Mesoporous Mater. 120, 460–466.

Mclintoc, I.S., 1967. Elovich equation in chemisorption kinetics. Nature 216, 1204–1205.

Menendez, I., Fuertes, A.B., 2001. Aging of carbon membranes under different environments. Carbon 39, 733–740.

Mulder, M., 2000. Basic Principles of Membrane Technology, 2nd ed. Kluwer Academic Publishers, Dordrecht.

Nguyen, C., Do, D.D., 1999. Adsorption of supercritical gases in porous media: determination of micropore size distribution. J. Phys. Chem. B 103, 6900–6908.

Nguyen, C., Do, D.D., Haraya, K., Wang, K., 2003. The structural characterization of carbon molecular sieve membrane (CMSM) via gas adsorption. J. Membr. Sci. 220, 177–182.

Okamoto, K., Kawamura, S., Yoshino, M., Kita, H., 1999. Olefin/paraffin separation through carbonized membranes derived from an asymetric polyimide hollow fiber membrane. Ind. Eng. Chem. Res. 38, 4424–4432.

Park, H.B., Jung, C.H., Kim, Y.K., Nam, S.Y., Lee, S.Y., Lee, Y.M.,2004. Pyrolytic carbon membranes containing silica derived from poly(imide siloxane): the effect of siloxane chain length on gas transport behavior and a study on the separation of mixed gases. J. Membr. Sci. 235, 87–98.

Park, H.B., Lee, S.Y., Lee, Y.M., 2005. Pyrolytic carbon membranes containing silica: morphological approach on gas transport behavior. J. Mol. Struct. 739, 179–190.

Reid, C.R., Thomas, K.M., 1999. Adsorption of gases on a carbon molecular sieve used for air separation: linear adsorptives as probes for kinetic selectivity. Langmuir 15, 3206–3218.

Robeson, L.M., 1991. Correlation of separation factor versus permeability for polymeric membranes. J. Membr. Sci. 62, 165–185.

Robeson, L.M., 2008. The upper bound revisited. J. Membr. Sci. 320, 390–400.

Rungta, M., Xu, L., Koros, W.J., 2012. Carbon molecular sieve dense film membranes derived from Matrimid® for ethylene/ethane separation. Carbon 50, 1488–1502.

Rutherford, S.W., Coons, J.E., 2005. Adsorption equilibrium and transport kinetics for a range of probe gases in Takeda 3A carbon molecular sieve. J. Colloid Interface Sci. 284, 432–439.

Rutherford, S.W., Do, D.D., 2000. Characterization of carbon molecular sieve 3A. Langmuir 16, 7245–7254.

Saufi, S.M., Ismail, A.F., 2004. Fabrication of carbon membranes for gas separation – a review. Carbon 42, 241–259.

Singh, A., Koros, W.J., 1996. Significance of entropic selectivity for advanced gas separation membranes. Ind. Eng. Chem. Res. 35, 1231–1234.

Stoeckli, F., Centeno, T.A., 1997. On the characterization of microporous carbons by immersion calorimetry alone. Carbon 35, 1097–1100.

Stoeckli, F., Slasli, A., Hugi-Cleavy, D., Guillot, A., 2002. The characterization of microporosity in carbons with molecular sieve effects. Microporous Mesoporous Mater. 51, 197–202.

Teixeira, M., Campo, M.C., Tanaka, D.A., Tanco, M.A., Magen, C., Mendes, A., 2011. Composite phenolic resin-based carbon molecular sieve membranes for gas separation. Carbon 49, 4348–4358.

Teixeira, M., Campo, M.C., Tanaka, D.A., Tanco, M.A., Magen, C., Mendes, A., 2012. Carbon–Al2O3–Ag composite molecular sieve membranes for gas separation. Chem. Eng. Res. Des. 90, 2338–2345.

Xiao, Y.C., Chng, M.L., Chung, T.S., Toriida, M., Tamai, S., Chen, H.M., Jean, Y.C.J., 2010. Asymmetric structure and enhanced gas separation performance induced by in situ growth of silver nanoparticles in carbon membranes. Carbon 48, 408–416.

Yin, X.Y., Wang, J.Q., Chu, N.B., Yang, J.H., Lu, J.M., Zhang, Y., Yin, D.H., 2010. Zeolite L/carbon nanocomposite membranes on the porous alumina tubes and their gas separation properties. J. Membr. Sci. 348, 181–189.

Yoda, S., Hasegawa, A., Suda, H., Uchimaru, Y., Haraya, K., Tsuji, T., Otake, K., 2004. Preparation of a platinum and palladium/polyimide nanocomposite film as a precursor of metal-doped carbon molecular sieve membrane via supercritical impregnation. Chem. Mater. 16, 2363–2368.

Yoshimune, M., Fujiwara, I., Suda, H., Haraya, K., 2006. Gas transport properties of carbon molecular sieve membranes derived from metal containing sulfonated poly(phenylene oxide). Desalination 193, 66–72.

Zeng, C.F., Zhang, L.X., Cheng, X.H., Wang, H.T., Xu, N.P., 2008. Preparation and gas permeation of nano-sized zeolite NaA-filled carbon membranes. Sep. Purif. Technol. 63, 628–633.

*Fig. 1 – Picture of a supported c-CMSM.*

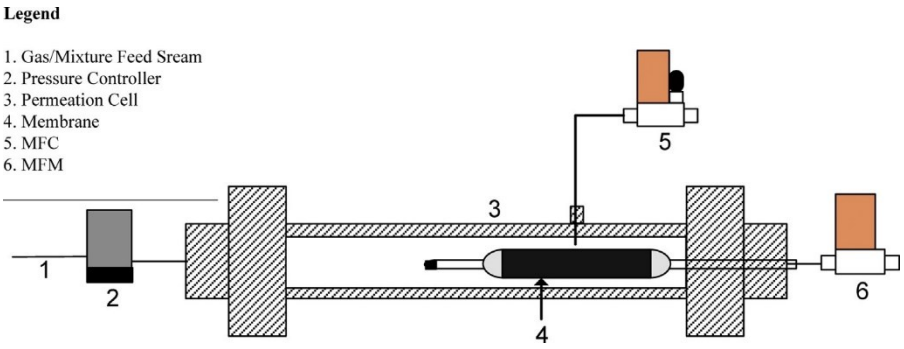


*Fig. 2 – Scheme depicting the permeation setup.*

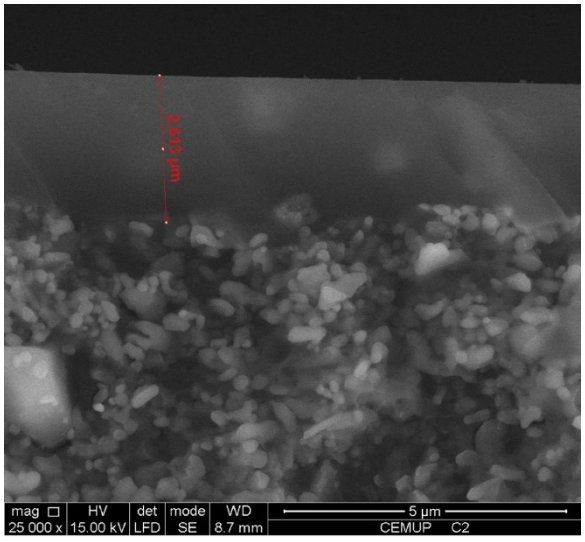


*Fig. 3 – SEM image of the cross-section of membrane M1, after carbonization (10,000× magnification).*

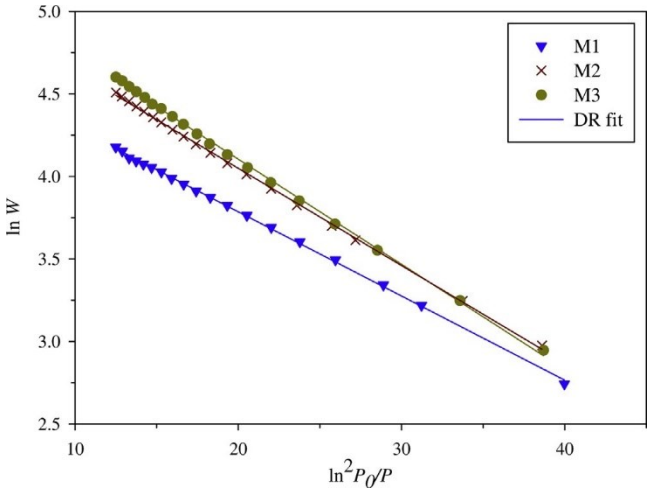


*Fig. 4 – $CO_2$ characteristic curves for the c-CMSM at 273 K (points – experimental data; line – DR fitting). The coefficients of determination ($R^2$) were 0.999, 0.991 and 0.999 for M1, M2 and M3, respectively.*

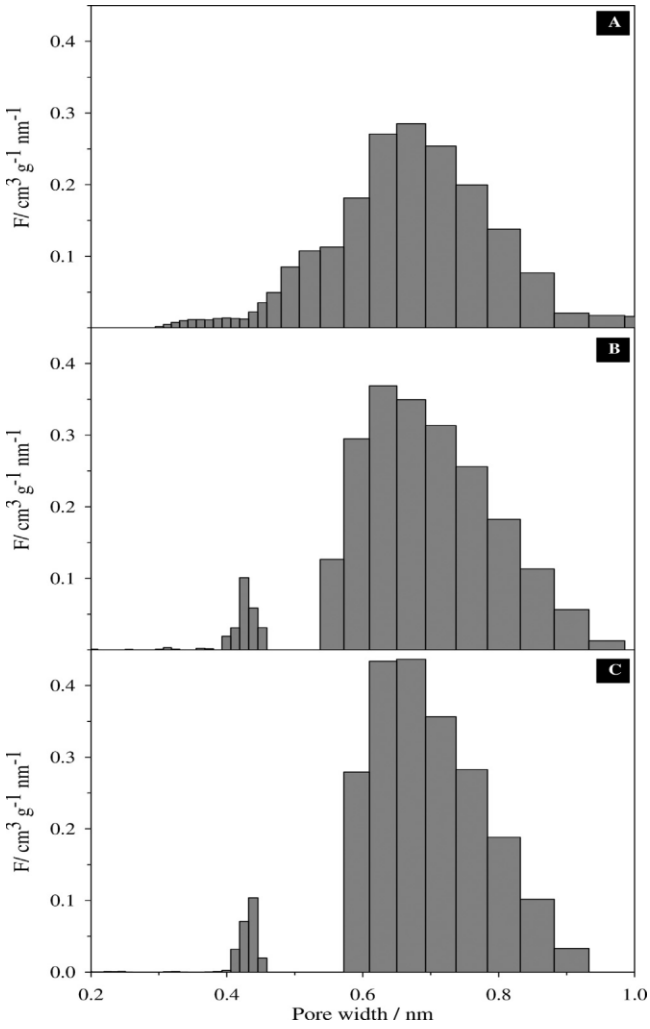


*Fig. 5 – Micropore size distribution of the composite membranes (M1-(A); M2-(B); M3-(C)).*

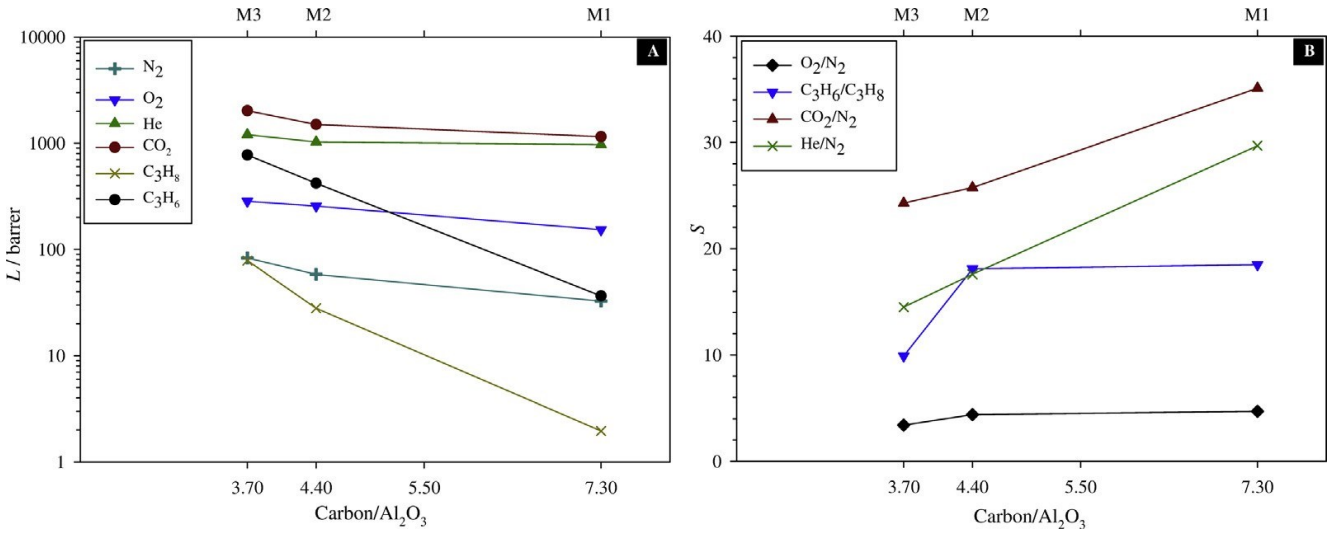


*Fig. 6 – Dependence of the membrane permeabilities (A) and ideal selectivities (B) with the carbon/Al2O3 ratio. Lines are used for readability.*

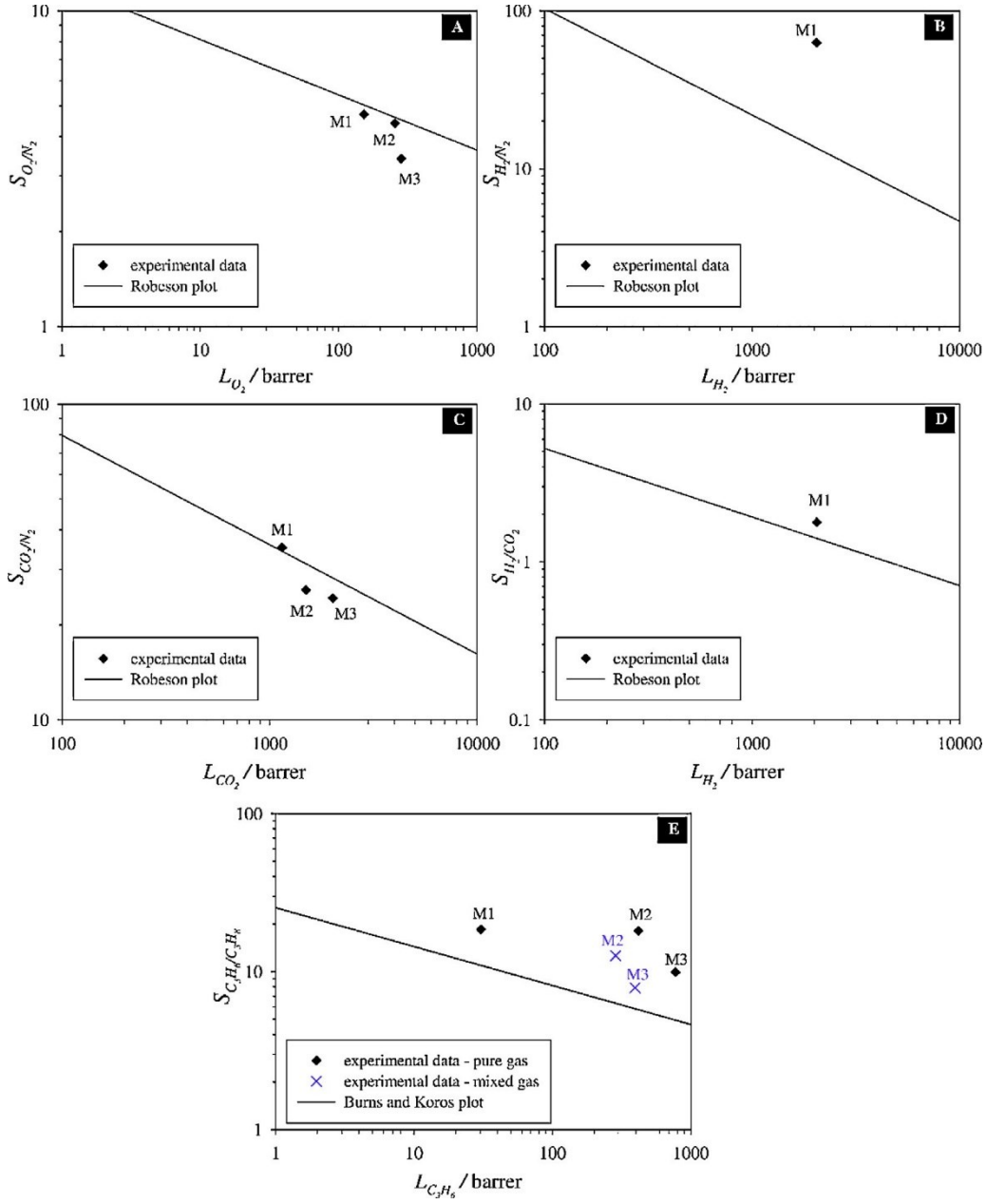


*Fig. 7 – Comparison of permeation results of the membranes with upper bound curves for $O_2/N_2$ (A), $H_2/N_2$ (B), $CO_2/N_2$ (C), $H_2/CO_2$ (D) and $C_3H_6/C_3H_8$ (E) separations (Robeson, 2008; Burns and Koros, 2003).*

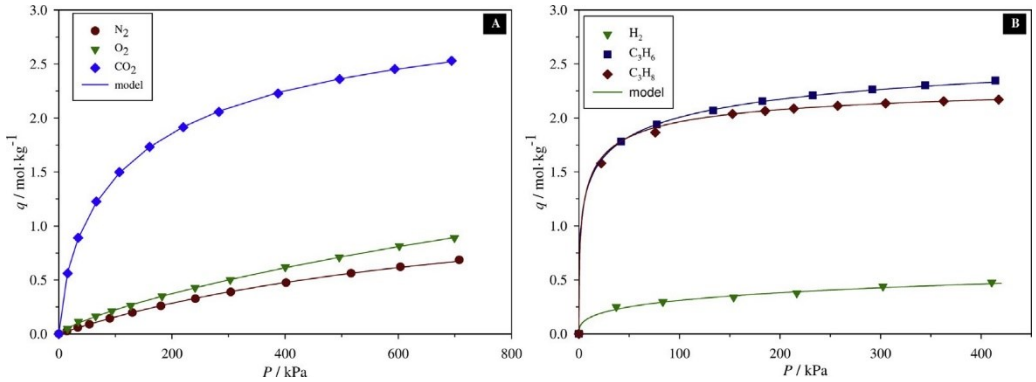


*Fig. 8 – Adsorption isotherms of $N_2$, $O_2$ and $CO_2$ (A) and $H_2$, $C_3H_6$ and $C_3H_8$ (B) at 293 K and corresponding fittings. The experimental values are represented by symbols and the SIPS fit model by lines.*

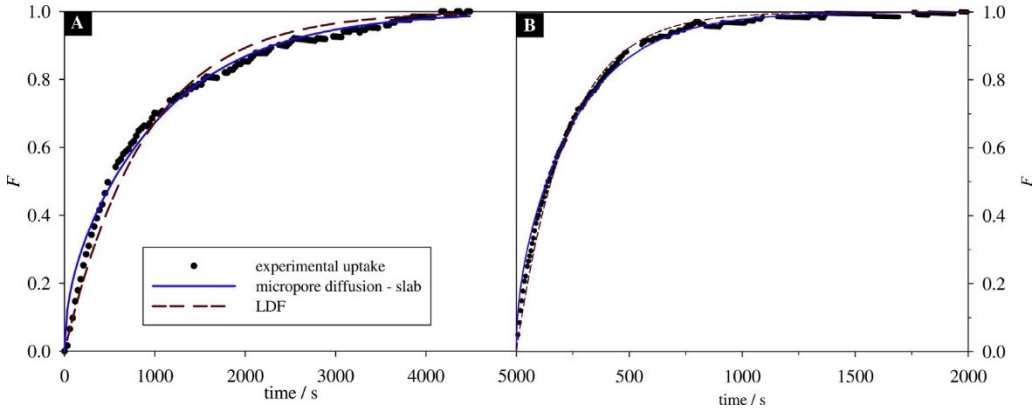


*Fig. 9 – Experimental and model fittings for the uptake curves of $N_2$ at P = 15 kPa (A) and $O_2$ at P = 35 kPa (B) (micropore diffusion model-solid lines; LDF model-dotted lines).*

*Fig. 10 – Uptake chemisorption history of O2 for three different pressure values; symbols-experimental data; lines-Elovich kinetic law ($1.31 < \xi < 4.49$; $2.7 \times 10–6 < \xi < 1.8 \times 10–5$ s–1).*

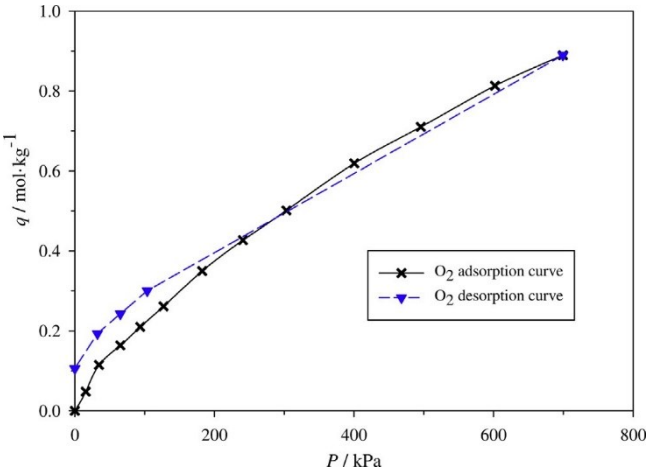


*Fig. 11 – $O_2$ adsorption/desorption equilibrium isotherm at 293 K.*

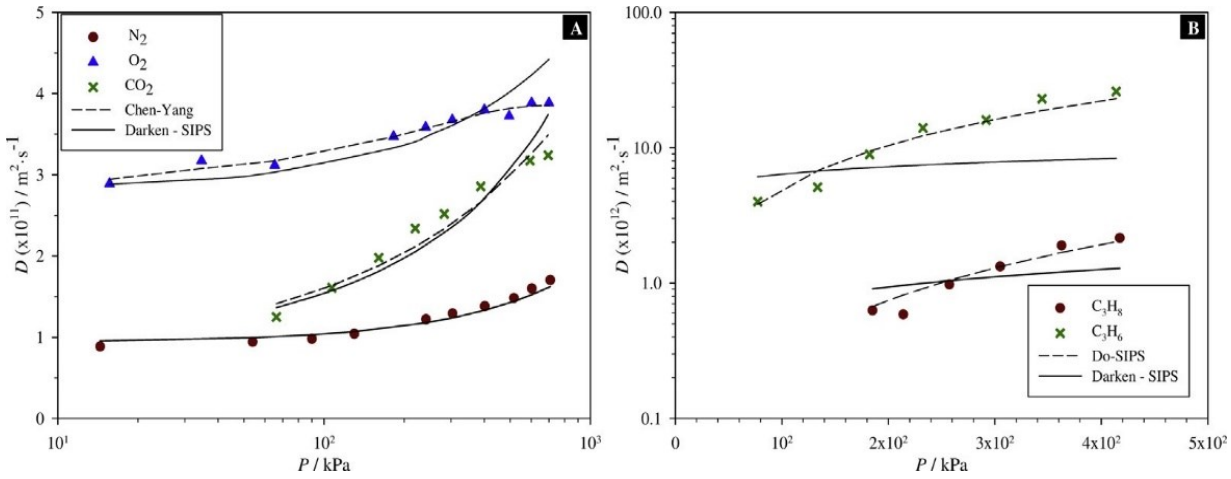


*Fig. 12 – Pressure-dependence of the diffusivities of $N_2$, $O_2$ and $CO_2$ (A) and $C_3H_6$ and $C_3H_8$ (B); symbols-experimental diffusivities; lines-fitting models ($D^{N2} = 9.2 \times 10^{-12}$; $D^{O2} = 2.9 \times 10^{-11}$, $\lambda = 1.6$; $D^{CO2} = 8.2 \times 10^{-12}$, $\lambda = 0.6$; $D^{C3H6} = 4.3 \times 10^{-13}$; $D^{C3H8} = 2.3 \times 10^{-15}$).*

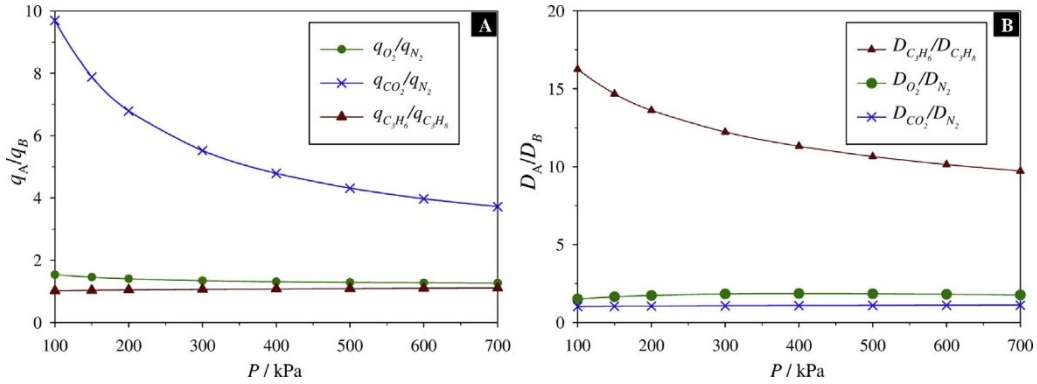


*Fig. 13 – Adsorption (a) and diffusion coefficients (b) ratio for the gas pairs $O_2/N_2$, $CO_2/N_2$ and $C_3H_6/C_3H_8$ as a function of the pressure. Lines were added for readability.*

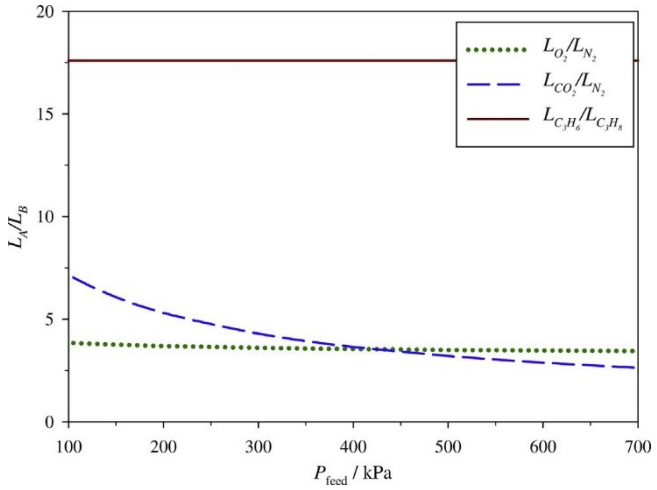


*Fig. 14 – Predicted permselectivities of c-CMSM M1 as a function of feed pressure (permeate pressure = 100 kPa).*

**Table 1 – Composition of the precursors used to prepare the c-CMSM.**

| Membrane | Phenolic resin (wt.%) | Boehmite (wt.%) |
|---|---|---|
| M1 | 12.5 | 0.50 |
| M2 | 15.0 | 1.0 |
| M3 | 12.5 | 1.2 |

**Table 2 – Burn off of M1, M2 and M3 in a 293–1173 K run under $N_2$ atmosphere.**

| Membrane | Precursor composition (wt.%) | | c-CMSM composition (wt.%) | | | Burn off (%) |
|---|---|---|---|---|---|---|
| | Resin | Boehmite | Carbon | $\gamma$-$Al_2O_3$ | C/$Al_2O_3$ | |
| M1 | 12.5 | 0.50 | 88.0 | 12.0 | 7.3 | 50.7 |
| M2 | 15.0 | 1.0 | 81.5 | 18.5 | 4.4 | 49.2 |
| M3 | 12.5 | 1.2 | 78.6 | 21.4 | 3.7 | 48.5 |

**Table 3 – Structural parameters determined from the DR fit and the Stoeckli correlation.**

| Parameter | M1 | M2 | M3 |
|---|---|---|---|
| $W_0$ ($cm^3\,g^{-1}$) | 0.123 | 0.187 | 0.217 |
| $E_0$ ($kJ\,mol^{-1}$) | 28.4 | 26.4 | 25.4 |
| l (nm) | 0.637 | 0.722 | 0.774 |

**Table 4 – Permeability of membranes M1–M3 toward probe gases at 293 K (feed pressure = 400 kPa; permeate pressure = 100 kPa).**

| Membrane | Permeability (barrer) | | | | | | |
|---|---|---|---|---|---|---|---|
| | $N_2$ | $O_2$ | He | $H_2$ | $CO_2$ | $C_3H_8$ | $C_3H_6$ |
| M1 | 32.7 | 153 | 971 | 2047 | 1148 | 1.96 | 36.2 |
| M2 | 58.2 | 256 | 1024 | – | 1499 | 28 | 420 |
| M3 | 83 | 284 | 1200 | – | 2017 | 78.5 | 776 |

**Table 5 – Ideal selectivity of membranes M1–M3 for gas pairs of interest at 293 K (feed pressure = 400 kPa; permeate pressure = 100 kPa).**

| Membrane | Ideal selectivity | | | | | | |
|---|---|---|---|---|---|---|---|
| | $O_2/N_2$ | $CO_2/N_2$ | $He/N_2$ | $H_2/N_2$ | $H_2/O_2$ | $H_2/CO_2$ | $C_3H_6/C_3H$ |
| M1 | 4.7 | 35.1 | 29.7 | 65.6 | 13.4 | 1.8 | 18.5 |
| M2 | 4.4 | 25.8 | 17.6 | – | – | – | 18.1 |
| M3 | 3.4 | 24.3 | 14.5 | – | – | – | 9.9 |

**Table 6 – Fitting parameters of the adsorption experimental data with the Langmuir and SIPS equations and corresponding fitting errors and MSC values.**

| Model | Parameter | $N_2$ | $O_2$ | $CO_2$ | $H_2$ | $C_3H_6$ | $C_3H_8$ |
|---|---|---|---|---|---|---|---|
| Langmuir | $q^{max}$ ($mol\,kg^{-1}$) | 1.47 | 1.35 | 2.57 | 0.46 | 2.39 | 2.25 |
| | $b$ ($kPa^{-1}$) | $1.2 \times 10^{-3}$ | $2.1 \times 10^{-3}$ | $1.6 \times 10^{-2}$ | $2.6 \times 10^{-2}$ | $6.3 \times 10^{-2}$ | $6.0 \times 10^{-2}$ |
| | *Err* | $1.4 \times 10^{-4}$ | $7.3 \times 10^{-3}$ | $3.1 \times 10^{-3}$ | $3.4 \times 10^{-3}$ | $3.3 \times 10^{-4}$ | $1.4 \times 10^{-6}$ |
| | MSC | 7.56 | 3.69 | 3.33 | 0.85 | 2.35 | 4.66 |
| SIPS | $q^{max}$ ($mol\,kg^{-1}$) | 1.62 | 2.35 | 3.28 | 1.71 | 3.47 | 2.42 |
| | $b$ ($kPa^{-1}$) | $1.0 \times 10^{-3}$ | $7.5 \times 10^{-4}$ | $7.4 \times 10^{-3}$ | $1.2 \times 10^{-4}$ | $2.9 \times 10^{-2}$ | 0.19 |
| | $n$ | 1.02 | 1.17 | 1.37 | 2.98 | 3.36 | 2.03 |
| | *Err* | $6.0 \times 10^{-5}$ | $2.5 \times 10^{-4}$ | $3.1 \times 10^{-5}$ | $7.3 \times 10^{-4}$ | $1.8 \times 10^{-6}$ | $7.1 \times 10^{-8}$ |
| | MSC | 9.17 | 4.99 | 7.95 | 2.27 | 8.22 | 7.45 |

**Table 7 – Permeabilities and permselectivities of membrane M1 toward $O_2$, $N_2$, $CO_2$, $C_3H_6$ and $C_3H_8$ determined by permeation and predicted from adsorption/diffusion experiments (293 K, feed pressure 400 kPa and permeate pressure 100 kPa).**

| Method | Permeability (barrer) | | | | | Ideal selectivities (S) | | |
|---|---|---|---|---|---|---|---|---|
| | $N_2$ | $O_2$ | $CO_2$ | $C_3H_8$ | $C_3H_6$ | $O_2N_2$ | $CO_2/N_2$ | $C_3H_6/C_3H_8$ |
| Permeation (exp.) | 32.7 | 153 | 1148 | 1.96 | 36.2 | 4.7 | 35.1 | 18.5 |
| Adsorption (predicted) | 52.3 | 176 | 154 | 2.67 | 50.6 | 3.4 | 2.9 | 18.9 |